

Cumulative Effects in 100 kHz Repetition-Rate Laser-Induced Plasma Filaments in Air

Tie-Jun Wang, Mehdi H. Ebrahim, Ivi Afxenti, Dionysis Adamou, Adetunmise C. Dada, Ruxin Li, Yuxin Leng, Jean-Claude Diels, Daniele Faccio, Arnaud Couairon, Carles Milián, and Matteo Clerici*

Cumulative effects are crucial for applications of laser filaments, such as for the remote transfer of energy and the control of electric discharges. Up to now, studies of cumulative effects in the air of high-repetition-rate pulse trains have been performed at lower rates than 10 kHz. Herein, the nonlinear effects associated with short plasma filaments produced by pulses of moderate energy (0.4 mJ per pulse) and repetition rates up to 100 kHz are experimentally characterized. With increasing repetition rate, a decrease in absorption, fluorescence emission, and breakdown voltage and concurrently an increase in peak intensity and third-harmonic-generation efficiency are observed. Hydrodynamic simulations of the heated gas show that the observed decreases are directly related to a quasi-stationary state of reduced gas density in the filament. However, further investigations are required to fully understand the physics underpinning the observed sharp reduction of the breakdown voltage at 100 kHz repetition rates. The results may prove relevant for energy and information delivery applications by laser-induced air waveguide or electric discharge and lightning control.


1. Introduction

When ultrashort intense laser pulses propagate in optically transparent media, such as in air, intensity-dependent nonlinear effects, for example, Kerr focusing, absorption, and gas ionization, lead to pulse reshaping and the formation of filaments, which can sustain nonlinear effects over several tens of meters.^[1,2] Laser filamentation in ambient air has attracted considerable attention in recent years owing to its central role in several applications, such as the formation of stationary localized waves,^[3] electric-discharge steering,^[4–6] machining,^[7] control and guiding of lightning,^[8–11] atmospheric control,^[12–14] remote sensing,^[15–17] pulse compression,^[18] optical communication,^[19–22] and the generation of coherent radiation in hardly accessible spectral regions such as the deep UV and THz.^[23–29] Filaments modify the gas density in which they propagate through different nonlinear light–matter interaction pathways, such as by excitation of molecular

T.-J. Wang, R. Li, Y. Leng
State Key Laboratory of High Field Laser Physics
Shanghai Institute of Optics and Fine Mechanics and CAS Centre for
Excellence in Ultra-intense Laser Science
Chinese Academy of Sciences
Shanghai 201800, China

T.-J. Wang, R. Li, Y. Leng
Center of Materials Science and Optoelectronics Engineering
University of Chinese Academy of Sciences
Beijing 100049, China

M. H. Ebrahim, I. Afxenti, D. Adamou, A. C. Dada, M. Clerici
James Watt School of Engineering
University of Glasgow
G12 8QQ Glasgow, UK
E-mail: matteo.clerici@glasgow.ac.uk

 The ORCID identification number(s) for the author(s) of this article can be found under <https://doi.org/10.1002/adpr.202200338>.

© 2023 The Authors. Advanced Photonics Research published by Wiley-VCH GmbH. This is an open access article under the terms of the Creative Commons Attribution License, which permits use, distribution and reproduction in any medium, provided the original work is properly cited.

DOI: 10.1002/adpr.202200338

A. C. Dada, D. Faccio
School of Physics and Astronomy
University of Glasgow
G12 8QQ Glasgow, UK

J.-C. Diels
School of Optical Science and Engineering and Department of Physics and
Astronomy
University of New Mexico
Albuquerque, New Mexico 87106, USA

A. Couairon
Centre de Physique Théorique
CNRS
École Polytechnique
Institut Polytechnique de Paris
F-91128 Palaiseau, France

C. Milián
Institut Universitari de Matemàtica Pura i Aplicada
Universitat Politècnica de València
46022 València, Spain

dynamics.^[30,31] However, the most significant gas density change comes from the photoinduced plasma's thermalization.^[1] The gas ionization concurrent with the filament formation develops over the short (nanosecond) time scale of electron recombination.^[32] In contrast, the gas hydrodynamics evolves at the rate of air molecules' thermal diffusion, that is, for up to milliseconds. This long-lasting effect is responsible for the low-density gas channel that accompanies filamentation^[33–35] and plays a dominant role in the triggering and steering of high-voltage discharges and lightning control.^[36–39] The temporary reduction of the density was also shown to enable energy transfer via air–waveguide guided lasers,^[34] to open communication channels through fog,^[19,20] and may be employed to improve remote spectroscopy.^[40] Common sources employed for filamentation are Ti:Sapphire-amplified lasers with high pulse energies (>10 mJ) and low repetition rates (≤ 1 kHz). In these conditions, thermal, acoustic, and plasma-mediated pulse-to-pulse interactions are highly suppressed. Such effects have, however, been observed in those cases where gas ionization or molecular alignment can be induced at the microjoule levels, as they can be readily operated at megahertz repetition rates. One relevant case is gas-filled hollow-core photonic-crystal fibers, where inter-pulse interactions have been observed at repetition rates as low as 50 kHz.^[41] There have been interesting recent studies of the evolution of the atmosphere following the passage of a filament. Most of these studies probed the atmosphere in the millisecond time span following filamentation. A radial shock wave leaves behind a depleted density distribution that has been exploited for guiding an auxiliary beam.^[42] Cumulative effects on the electric breakdown have been reported at a 1 kHz repetition rate, highlighting the role of long-lived oxygen ions.^[43] The cumulative effect of pulses separated by 1 ms has also been recently investigated by Isaacs et al.^[44] There is, however, a qualitative and quantitative difference between cumulative effects at 1, 10, and 100 kHz. It has been known since 2012 that filaments produced by a train of pulses at 10 kHz are considerably longer and have a brighter conical emission than observed at 1 kHz.^[45,46] Between 10 and 100 kHz, there is clearly a change in shock wave physics. Shadowgraphy performed on filaments has shown the shock wave velocity switching from supersonic to sonic 6 μ s after the passage of the ionizing pulse.^[47] With high-energy, ultrashort, high-repetition-rate Yb-based laser systems now becoming more widespread, investigations on cumulative effects at repetition rates into the kHz range have started. For instance, effects on THz generation^[48] and wake dynamics^[49] have been recently reported.

Here, we consider the intermediate case of moderate energies (≈ 0.4 mJ) and high repetition rates (up to 100 kHz), and we analyze cumulative effects on energy deposition, nonlinear phenomena, and direct current air breakdown. Using a hydrodynamic gas model, we elucidate the gas density's role in the observed effects.

2. Results

2.1. Energy Deposition and Gas Dynamics

The experiments were conducted using a Yb:KGW-amplified laser (Carbide 40 W, Light Conversion) with a central wavelength

of 1028 nm, tunable pulse repetition (sub-harmonics of 100 kHz), pulse energy of ≈ 0.4 mJ, and pulse duration of ≈ 240 fs. A sketch of the experimental setup is shown in **Figure 1a**. A linearly polarized beam with a half-width at $1/e$ (HW $1/e$) of 1168 ± 6 μ m was focused by a lens (L_1) with a focal length of $f_1 = 15$ cm, to generate a plasma filament in the air. To measure the energy deposited into the gas system by the filament at different laser repetition rates, the region between L_1 and L_4 was enclosed in a vacuum tube with input- and output-fused silica optical windows (antireflection-coated 1 mm thick). The pulse energy under the focus was measured with a calibrated photodiode (Pd) in the case of air at atmospheric pressure ($< 10^{-3}$ mbar, U_V) and under vacuum conditions ($< 10^{-3}$ mbar, U_V). This way, we removed calibration uncertainties and other sources of losses that arise from measuring the energy before and after the focus. During the experiments, the pulse energy before the focus was kept constant while changing the repetition rate. The beam size variation with the repetition rate is $< 2\%$ over all the tested conditions. The relative energy loss $\eta = (1 - U_G/U_V) \times 100$ across the beam focus is shown in **Figure 1b** for two different input pulse energies ($U_{in} = 400$ and 300 μ J) and increasing laser repetition rate. For the higher input energy case, there is an evident decrease in the energy deposited in the gas at increasing repetition rates, going from

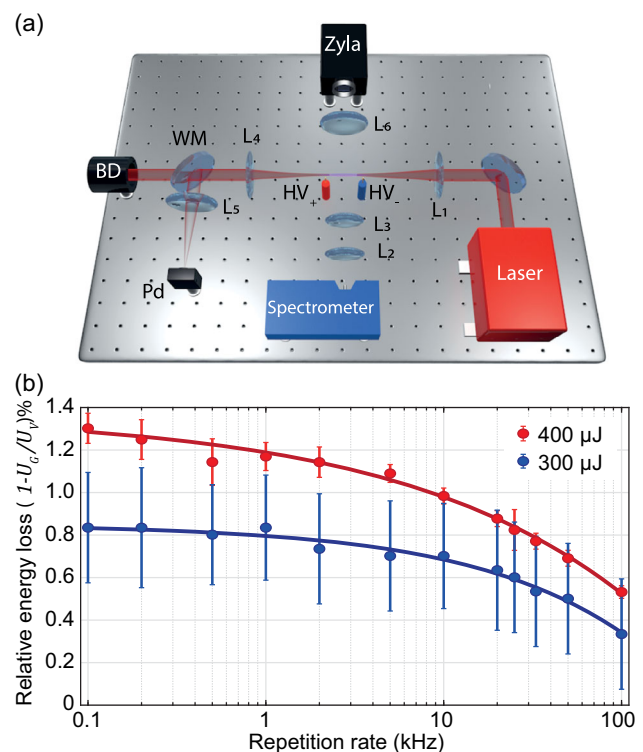


Figure 1. a) Schematic of experimental setup. Pd is a photodiode detector. L_1 – L_5 are positive lenses with focal lengths of 15, 5, 10, 15, and 10 cm, respectively. L_5 is an $f/2.0$, 25 mm equivalent focal length camera lens (Thorlabs MVL25M43). WM and BD are a wedge mirror and a beam dump, respectively. b) Relative energy loss $(1 - U_G/U_V) \times 100$ as a function of the laser repetition rate (logarithmic scale) and for two different pulse energies (400 μ J in red, 300 μ J in blue). The solid curves are a guide for the eye obtained by fitting the experimental data with a power function.

nearly 1.3% at 100 Hz to nearly 0.55% at 100 kHz. A similar trend is also recorded at lower energies, yet with more modest changes. Losses in the focus result from nonlinear light-matter interaction, including multiphoton absorption and scattering from the photoinduced plasma. The nonlinear nature of the losses is evident from the difference in the relative energy loss η between the $U_{in} = 400$ and $300 \mu\text{J}$ cases.

We link the reduction of nonlinear losses to the decrease of the gas density, a consequence of the volume heating. To support this claim, we have performed hydrodynamic simulations of the laser-heated gas volume at different values of absorbed energy to calculate the steady-state gas volume density. To this end, we solved the compressible fluid Euler equations in 2D cylindrical coordinates (neglecting the azimuthal dynamics) with a source term and accounting for temperature diffusion. The numerical integration is performed following Refs. [50,51]. Details of the model are reported elsewhere (e.g., in the Supplementary Materials of Ref. [6]). The numerical model considers an initially heated gas consequent from the absorption of the energy deposited by the first optical pulse ΔU_0 , and then

assumes that the energy deposited by successive pulses is proportional to the instantaneous gas density. **Figure 2a** is representative of the gas density dynamics for three different repetition rates and assuming $\Delta U_0 = 0.5 \mu\text{J}$ employed to heat a 1.5 mm long (length of the plasma filaments, see **Figure 2c**) and $40 \mu\text{m}$ diameter (beam waist) gas cylinder. **Figure 2b** shows how an almost steady state is achieved for the gas density at the high 100 kHz repetition rate.

To provide a point of comparison between the model results and experimental data, we considered the simple assumption that absorption has a density-dependent component as $U_{out}(R) = U_{in} - \kappa U_{in} - \delta(R) U_{in}$, where U_{out} is energy of pulse after filamentation, $\delta(R) = \alpha \rho(R)$ is a density (ρ)-dependent component which varies with repetition rate R , and κ is a constant pertaining to a fixed loss component. Thus, the relative energy loss, as found experimentally in **Figure 1b**, can be written as $\eta(R) = 1 - U_{out}(R)/U_{in} = \alpha[\rho(R) - \rho_0] + \eta_0$, where $\rho(R)$ is the density which we calculated via the hydrodynamic simulations in the steady state and on axis, ρ_0 is the density of the unperturbed gas, and $\eta_0 = \kappa + \alpha\rho_0$ captures losses that are not dependent on

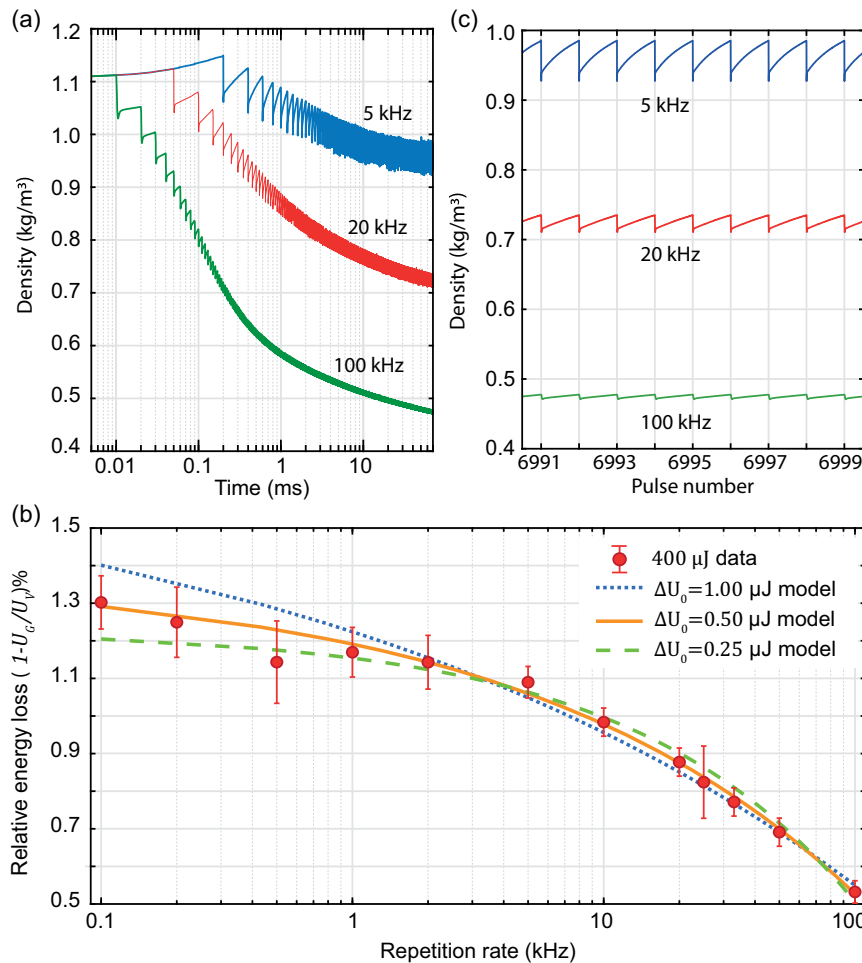


Figure 2. a) Numerical simulation of the gas density dynamics for an initial $\Delta U_0 = 0.5 \mu\text{J}$ energy deposited as heat into the gas, and for three different repetition rates. b) Comparison between gas density dynamics after several pulses for the three repetition rates shown in (a), highlighting the onset of a quasi-stationary condition at 100 kHz. c) Comparison between experimental data, same as in **Figure 1c**, and the results from the predictions from the hydrodynamic gas model for three different initial energies heating the gas.

the repetition rate. We investigated the relative loss for a range of initially absorbed energies (ΔU_0), that is, the energy the first pulse of the excitation train converted into heat, and found that the relative losses $\eta(R)$ match the values found experimentally, as shown in Figure 2c for $\Delta U_0 = 0.5 \mu\text{J}$. To perform the fit, α was considered a fitting parameter and η_0 was constrained by the experimental observations. Results of simulations performed with different initially absorbed energies are shown for comparison.

There is no direct measurement of ΔU_0 , the energy of the first pulse converted into heat. Our model matches the experimental data when 1/10th of the energy lost in the filamentation process at 100 Hz (when cumulative effects are negligible), that is, $\approx 5 \mu\text{J}$, is converted into heat. It is worth noting, however, that this value is strongly dependent on the geometry of the heated gas assumed in the model. There is significant uncertainty on the geometrical parameters defining the heated gas cylindrical region, and non-linear pulse propagation should be modeled to identify the heated volume properly. In addition, a full 3D + 1 hydrodynamic

simulation should be employed to allow for a quantitative comparison between simulations and our experimental results. Notwithstanding, the remarkable matching between the experimental data and our simplified model supports the claim that the repetition rate dependence of the energy lost by the plasma filament is a consequence of the decreased gas density driven by plasma-induced heating.

2.2. Filament Length

We have investigated the repetition rate dependence of the plasma filament length. The plasma-induced fluorescence was imaged on a CMOS camera (Zyla, Andor), and the input slit of a compact spectrometer (HR4000, Ocean Optics). The acquisition time for both instruments was changed with the repetition rate to record a cumulated signal from the same number of pulses. The images from the CMOS camera were then analyzed, and the results are shown in Figure 3. It can clearly be seen that at increasing repetition rates, the fluorescence signal

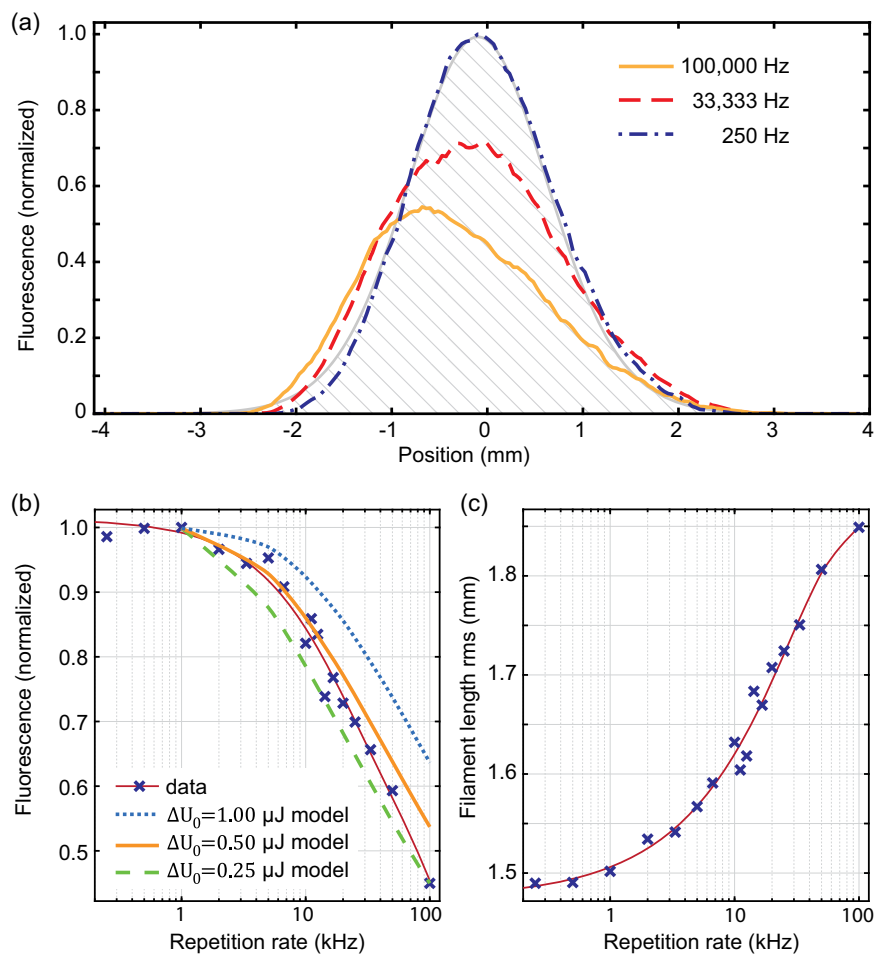


Figure 3. a) Spatially resolved fluorescence signal for three repetition rates. The signal is acquired by integrating the same number of pulses in all the cases. The shaded curve is the fluorescence profile expected from multiphoton absorption. The pulses propagate from negative to positive values of the horizontal axis. b) Integrated fluorescence signal for varying repetition rates (logarithmic scale). Results from the hydrodynamic model for three different initial heating energies are also shown. c) Filament length measured as the root-mean-square (rms) extension in the propagation direction of the fluorescence signal. The red curves in (b) and (c) are a guide for the eye obtained by a smoothing interpolant fit of the experimental data (dark blue crosses).

decreases—Figure 3a,b. At the same time, the filament is distorted further away from the focusing lens, resulting in a slight increase in the filament length—Figure 3c. The fluorescence signal for the low-repetition-rate case—blue dot-dashed curve in Figure 3a—matches the expected one considering a multiphoton absorption process with $I \propto I^k$ and $k=10$ ($U_{i,O_2} \simeq 12\text{eV}$, $h\nu \simeq 1.204\text{eV}$) and considering linear propagation ($\text{HW}1/e$ in the focus of $\sim 23\ \mu\text{m}$), depicted in Figure 3a with a grey curve and shaded area. The recorded decrease of the fluorescence signal with increasing repetition rates shown by the blue crosses with the red interpolant curve in Figure 3b matches the prediction of the hydrodynamic model—yellow curve in Figure 3b—for the same parameter $\Delta U_0 = 0.5\ \mu\text{J}$ that best fits the absorption losses described in Figure 2b. This comparison is made assuming that the fluorescence yield is proportional to the gas density. Results expected for the other two values of ΔU_0 are also shown in Figure 3b for comparison. The distortion along the propagation direction can be interpreted as the consequence of a nonuniform refractive index.

2.3. Fluorescence

A typical fluorescence spectrum acquired in a plane transverse to the propagation direction is shown in Figure 4a. Signatures from

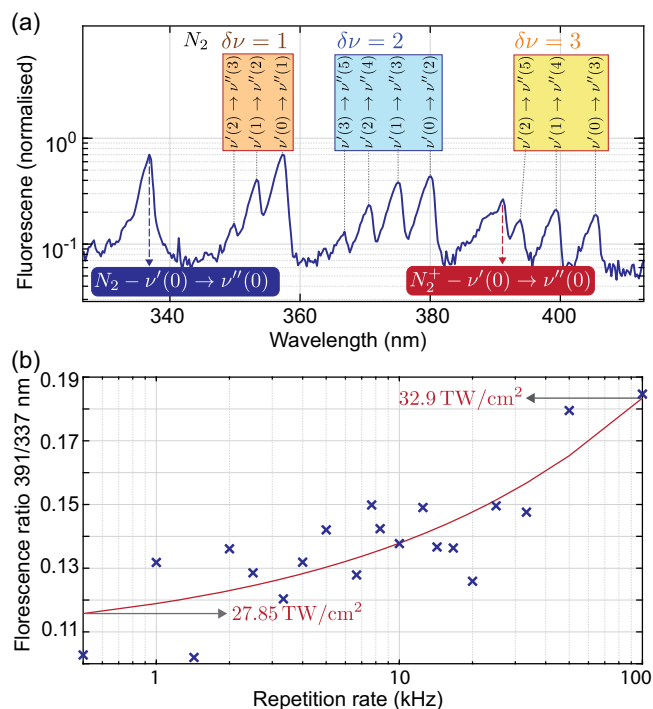


Figure 4. a) Spectrally resolved fluorescence signal (integrated along the direction transverse to the pulse propagation). b) Ratio of the fluorescence for the $\delta\nu = 0$ transition of the first band system of molecular nitrogen ions (nm) and that of the second positive band system of molecular nitrogen (nm), as a function of the laser repetition rate and for energies of $\mu\text{J}\ \text{pulse}^{-1}$. The red curve is a fit obtained considering a power dependence and serves as a guide for the eye. All the fluorescence signals are acquired over the same number of laser pulses.

transitions between vibrational levels in the second positive band system ($2P$) of molecular nitrogen ($C^3\Pi_u(v') \rightarrow B^3\Pi_u(v'')$) and from the first negative system ($1N$) of ionized nitrogen ($B^3\Sigma_u^+(v') \rightarrow X^2\Sigma_g^+(v'')$) are clearly visible. The main visible branches are for changes in the vibrational quantum numbers $\delta\nu = v'' - v' = 0, 1, 2$, and 3. The ratio G between the fluorescence yield for the $N_2^+(0 \rightarrow 0)$ transition, at $\simeq 391\ \text{nm}$ and that for $N_2(0 \rightarrow 0)$, at $337\ \text{nm}$, is proportional to the peak intensity of the radiation in the plasma filament according to the empirical relation $I_0 = 79 \times (2.6/G - 1)^{-0.34}\ (\text{TW}\ \text{cm}^{-2})$.^[52] We show in Figure 4b that such a ratio increases with the laser repetition rate, indicating an increase in the peak intensity inside filaments. According to the model provided earlier, the peak intensity increases from $\simeq 28\ \text{TW}\ \text{cm}^{-2}$ at $500\ \text{Hz}$ to $\simeq 33\ \text{TW}\ \text{cm}^{-2}$ at $100\ \text{kHz}$.

2.4. Spectral Broadening and Third Harmonic Generation

The reduction of energy deposition observed at increasing repetition rates should correspond to a decline of dissipative nonlinear effects, such as plasma generation by multiphoton ionization. Such effects are loss dependent, and we can, for instance, expect a reduction in the spectral blue shift induced by the time-varying plasma refractive index.^[53] We have recorded the input and output pulse spectra at varying repetition rates and constant pulse energies ($400\ \mu\text{J}$). For the spectral analysis, the beam was collimated and attenuated by Fresnel reflection from a pair of fused silica wedges and then injected into a spectrometer (Ocean Optics HR4000). We have measured the reduction of spectral shift $\Delta\lambda = \lambda_0^{\text{out}} - \lambda_0^{\text{in}}$, with λ_0 the center of mass wavelength, at varying laser repetition rates and the results are shown in Figure 5. At low, $500\ \text{Hz}$ repetition rates—Figure 5a—the pulse spectrum is blue shifted by nearly $1\ \text{nm}$. Increasing the repetition rate decreases the nonlinear spectral shift to almost cancel any reshaping for pulse trains at $100\ \text{kHz}$ —see Figure 5b. Figure 5c clearly highlights how the nonlinear pulse reshaping is quenched at increasing repetition rates. We interpret this effect as a consequence of the lower density of gas molecules resulting from the heated gas dynamics. We note that the spectral reshaping in our experimental conditions is minimal. This observation motivated the decision not to model the pulse propagation considering nonlinear effects, as they are expected to play a minor role in defining the pulse properties. This is further confirmed by the good match of the profile expected from multiphoton absorption (grey shaded) and the observed fluorescence signal (blue dot-dashed line) visible in Figure 3a.

Another significant observation concerns the generation of the third harmonic. Figure 5d shows how the third harmonic signal grows for increasing repetition rates and reaches a maximum conversion efficiency of $0.04\% \pm 0.02\%$. The third-harmonic-conversion efficiency has been measured by recording with a calibrated photodiode (Thorlabs, S120VC), the power of the $343\ \text{nm}$ radiation isolated using a fused silica-dispersing prism (Eksma, 320-1525). The increase in the signal of nearly a factor of 1.5 is quantitatively compatible with what is expected from the cubic dependence of the third harmonic from the pulse peak intensity and the intensity increase measured from the fluorescence signals detailed in Section 2.3 ($1.179^3 \simeq 1.64$).

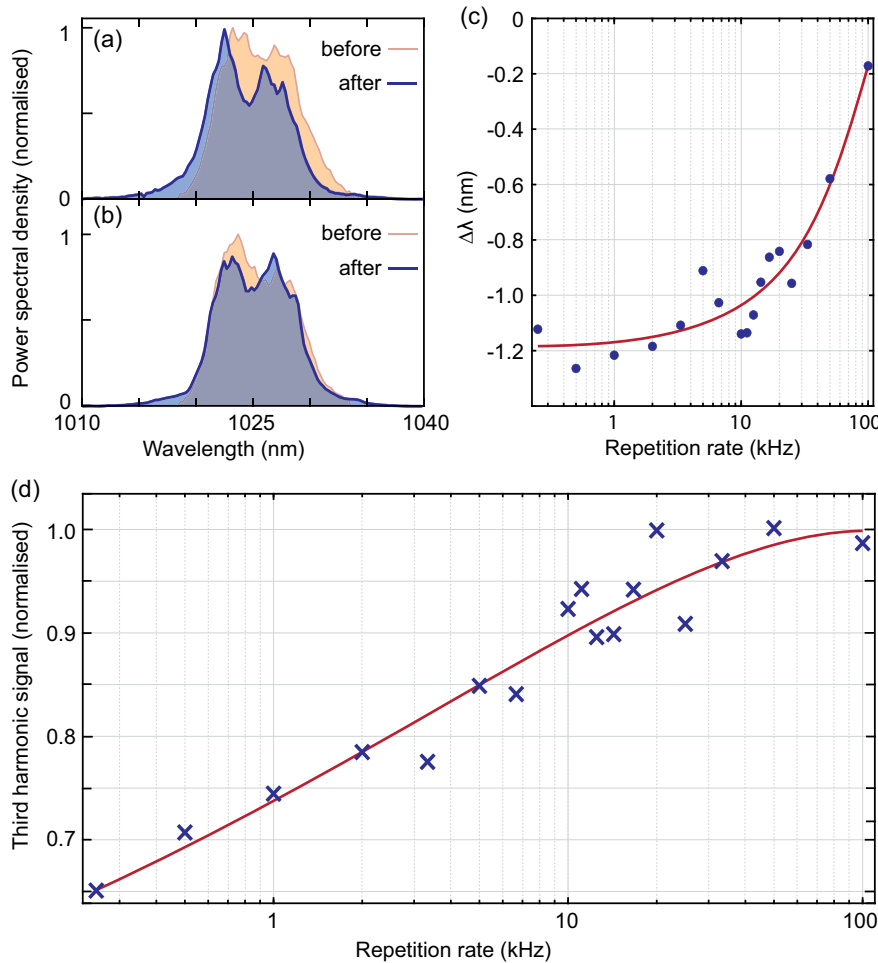


Figure 5. a,b) The pulse spectrum before (orange) and after (blue) the lens focus for Hz and kHz repetition rates, respectively. c) The shift of the center of weight wavelength of the pulse spectrum after the focus in function of the laser repetition rate (logarithmic scale). The red curve is a guide for the eye obtained with a power–law fit. d) The third-harmonic-signal function of the laser repetition rate. The red curve is a fit obtained considering a power dependence and serves as a guide for the eye. The maximum third-harmonic-generation efficiency was measured to be $0.04 \pm 0.02\%$.

2.5. Gas Breakdown

We finally investigated the pulse accumulation effect of laser-triggered air breakdown. In our experiment, two tip electrodes separated by 5 mm were used, and the natural breakdown discharge occurred at ≈ 6 kV. We investigated how the potential required for the dielectric breakdown depends on the pulse repetition rate for a fixed pulse energy of 400 μ J. The results are shown in **Figure 6**. While the overall breakdown field reduction is limited to $<5\%$ at low repetition rates, it increases significantly at 100 kHz, reaching a more significant 20%. To understand the observed dependence of the breakdown field from the repetition, we considered both geometrical factors and the gas hydrodynamics.

We have considered that the electrodes are slightly away from the filament axis and employed the radial-dependent density as a function of the repetition rate obtained from the hydrodynamic simulations discussed in Section 2.1 as a parameter in a model of the time-dependent carrier density. This way, we obtained the expected breakdown voltage as a function of the repetition rate

and at different distances from the filament axis. Specifically, we solved the following system of coupled ordinary differential equations with the simple assumption that breakdown arises when the electron density is nondecreasing with time. Toward that end, the dynamical continuity equations that govern the time evolution of electron (N_e), positive ion (N_p), and negative ion charge (N_n) densities are as follows ^[54]

$$\frac{\partial N_e}{\partial t} = \alpha N_e - \gamma N_e - \beta_{ep} N_e N_p \quad (1)$$

$$\frac{\partial N_p}{\partial t} = \alpha N_e - \gamma N_e - \beta_{ep} N_e N_p - \beta_{np} N_n N_p \quad (2)$$

$$\frac{\partial N_n}{\partial t} = \gamma N_e - \beta_{np} N_n N_p \quad (3)$$

where α , γ , β_{ep} , β_{np} are constants relating to the impact ionization, attachment, electron–ion recombination, and ion–ion recombination constants, respectively. Such transport parameters depend on the electric field (see Ref. [54]), and so does

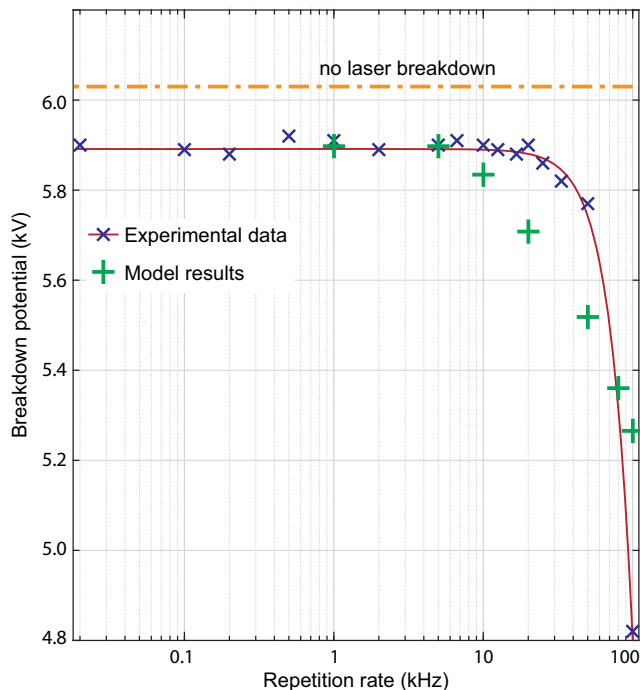


Figure 6. Breakdown potential for a 5 mm gap between needle-like electrodes without (orange dot-dashed line) and with laser pulses of 400 μ J at different repetition rates (blue crosses). The red curve is a fit obtained considering a power law and serves as a guide for the eye. The green crosses are the result of a numerically simulated breakdown potential as a function of the laser repetition rate and for 0.65 mm electrodes distance from the filament axis.

the time evolution of the charge densities. We note that avalanche effects are included in the model, as electrons are accelerated by the external field and gain average energy, which is accounted for through the field-dependent impact ionization rate α .

The model partially captures the value of the reduced breakdown voltage and qualitatively reproduces the experimental trend for an electrodes–filament radial distance of ≈ 0.65 mm, compatible with the experimental parameters. The orange curve in Figure 6 shows the best match obtained with our model. The model does not capture the fast decrease observed at 100 kHz, and our experimental facility does not allow us to investigate the breakdown effect at higher repetition rates and energies. Further studies may disclose key contributions from other physical effects, such as long-lived oxygen ions,^[43] which are not considered in our model.

3. Conclusion

Yb-based high-power ultrafast systems enable research in cumulative effects in filamentation at high, >10 kHz repetition rates, which were impossible or hardly feasible with Ti:Sapphire systems. We have investigated the regime of moderate energies enabled by our laser and identified key effects ensuing when the repetition rate is increased into the tens of kHz. Significantly, the

reduced density of the filamenting region leads to a quenching of nonlinear reshaping and losses. At the same time, intensity in the filament increases, and with that, the third-harmonic-generation efficiency. Interestingly, we observed a sharp reduction of the breakdown voltage as the repetition rate approached 100 kHz. This effect, which requires further experimental validation, possibly with higher energies and repetition rates, appears not to be a sole consequence of the reduced gas density, suggesting contributions from long-lived ions. Our results pave the way to further studies in nonlinear optics and atmospheric control with high-repetition-rate ultrafast lasers, to be further investigated with different laser systems, possibly at longer wavelengths, where the ionization processes are different and successive laser pulses interact more strongly with any residual ions.

Acknowledgements

TJW acknowledges the support from NSAF (Grant no. U2130123), Strategic Priority Research Program of the Chinese Academy of Sciences (Grant no. XDB16), International Partnership Program of Chinese Academy of Sciences (Grant nos. 181231KYSB20200033 and 181231KYSB20200040), Shanghai Science and Technology Program (Grant no. 21511105000), and Oversea Training Program of Ministry of Science and Technology. MC acknowledges the support from UK Research and Innovation (UKRI) and the UK Engineering and Physical Sciences Research Council (EPSRC) (Fellowship “In-Tempo” EP/S001573/1), and the Royal Society (RGS\R1\201365). JCD acknowledges the support of NASA (SBIR grant 80NSSC22PB067). The authors wish to acknowledge Drs. Jean-Pierre Wolf, Jerome Kasparian, Clara Saraceno, and Olga Kosareva for enlightening discussions.

Conflict of Interest

The authors declare no conflict of interest.

Data Availability Statement

All the data supporting the conclusions reported in this manuscript are available at <http://dx.doi.org/10.5252/gla.researchdata.1345>.

Keywords

filaments, fluorescence, high-repetition-rate, hydrodynamic models, light–matter interaction, plasma

Received: November 24, 2022
Revised: December 16, 2022
Published online: January 31, 2023

- [1] A. Couairon, A. Mysyrowicz, *Phys. Rep.* **2007**, 441, 47.
- [2] J.-C. Diels, M. C. Richardson, L. Arissian, in *Light Filaments: Structures, Challenges And Applications*, Institution of Engineering and Technology, UK **2021**.
- [3] D. Faccio, A. Averchi, A. Lotti, P. Di Trapani, A. Couairon, D. Papazoglou, S. Tzortzakos, *Opt. Express* **2008**, 16, 1565.
- [4] M. Rodriguez, R. Sauerbrey, H. Wille, L. Wöste, T. Fujii, Y.-B. André, A. Mysyrowicz, L. Klingbeil, K. Rethmeier, W. Kalkner, J. Kasparian, E. Salmon, J. Yu, J.-P. Wolf, *Opt. Lett.* **2002**, 27, 772.

- [5] B. Forestier, A. Houard, I. Revel, M. Durand, Y. B. André, B. Prade, A. Jarnac, J. Carbonnel, M. Le Nevé, J. C. de Miscault, B. Esmler, D. Chapuis, A. Mysyrowicz, *AIP Adv.* **2012**, 2, 012151.
- [6] M. Clerici, Y. Hu, P. Lasonde, C. Milián, A. Couairon, D. N. Christodoulides, Z. Chen, L. Razzari, F. Vidal, F. Légaré, D. Faccio, R. Morandotti, *Sci. Adv.* **2015**, 1, 1400111.
- [7] D. Kiselev, L. Woeste, J.-P. Wolf, *Appl. Phys. B* **2010**, 100, 515.
- [8] J.-C. Diels, R. Bernstein, K. E. Stahlkopf, X. M. Zhao, *Sci. Am.* **1997**, 277, 50.
- [9] J. Kasparian, R. Ackermann, Y.-B. André, G. Méchain, G. Méjean, B. Prade, P. Rohwetter, E. Salmon, K. Stelmaszczyk, J. Yu, A. Mysyrowicz, R. Sauerbrey, L. Woeste, J.-P. Wolf, *Opt. Express* **2008**, 16, 5757.
- [10] T. Produit, P. Walch, C. Herkommer, A. Mostajabi, M. Moret, U. Andral, A. Sunjerga, M. Azadifar, Y.-B. André, B. Mahieu, W. Haas, B. Esmler, G. Fournier, P. Krötz, T. Metzger, K. Michel, A. Mysyrowicz, M. Rubinstein, F. Rachidi, J. Kasparian, J.-P. Wolf, A. Houard, *Eur. Phys. J. Appl. Phys.* **2021**, 93, 10504.
- [11] A. Houard, P. Walch, T. Produit, V. Moreno, B. Mahieu, A. Sunjerga, C. Herkommer, A. Mostajabi, U. Andral, Y.-B. André, M. Lozano, L. Bizet, M. C. Schroeder, G. Schimmel, M. Moret, M. Stanley, W. A. Rison, O. Maurice, B. Esmler, K. Michel, W. Haas, T. Metzger, M. Rubinstein, F. Rachidi, V. Cooray, A. Mysyrowicz, J. Kasparian, J.-P. Wolf, arXiv 2207.03769, (2022).
- [12] P. Rohwetter, J. Kasparian, K. Stelmaszczyk, Z. Hao, S. Henin, N. Lascoux, W. M. Nakaema, Y. Petit, M. Queiße, R. Salamé, E. Salmon, L. Wöste, J.-P. Wolf, *Nat. Photonics* **2010**, 4, 451.
- [13] J. Ju, J. Liu, C. Wang, H. Sun, W. Wang, X. Ge, C. Li, S. L. Chin, R. Li, Z. Xu, *Opt. Lett.* **2012**, 37, 1214.
- [14] L. de la Cruz, E. Schubert, D. Mongin, S. Klingebiel, M. Schultze, T. Metzger, K. Michel, J. Kasparian, J.-P. Wolf, *Appl. Phys. Lett.* **2016**, 109, 251105.
- [15] J. Kasparian, M. Rodriguez, G. Méjean, J. Yu, E. Salmon, H. Wille, R. Bourayou, S. Frey, Y.-B. André, A. Mysyrowicz, R. Sauerbrey, J.-P. Wolf, L. Wöste, *Science* **2006**, 301, 61.
- [16] S. L. Chin, H. L. Xu, Q. Luo, F. Théberge, W. Liu, J. F. Daigle, Y. Kamali, P. T. Simard, J. Bernhardt, S. A. Hosseini, M. Sharifi, G. Méjean, A. Azarm, C. Marceau, O. Kosareva, V. P. Kandidov, N. Aközbek, A. Becker, G. Roy, P. Mathieu, J. R. Simard, M. Châteauneuf, J. Dubois, *Appl. Phys. B* **2009**, 95, 1.
- [17] H. Xu, Y. Cheng, S.-L. Chin, H.-B. Sun, *Laser Photon. Rev.* **2015**, 9, 275.
- [18] C. P. Hauri, W. Kornelis, F. W. Helbing, A. Heinrich, A. Couairon, A. Mysyrowicz, J. Biegert, U. Keller, *Appl. Phys. B* **2004**, 79, 673.
- [19] G. Schimmel, T. Produit, D. Mongin, J. Kasparian, J.-P. Wolf, *Optica* **2018**, 5, 1338.
- [20] M. C. Schroeder, I. Larkin, T. Produit, E. W. Rosenthal, H. Milchberg, J.-P. Wolf, *Opt. Express* **2020**, 28, 11463.
- [21] M. C. Schroeder, U. Andral, J.-P. Wolf, *AIP Adv.* **2022**, 12, 095119.
- [22] A. Goffin, J. Griff-McMahon, I. Larkin, H. M. Milchberg, arXiv 2203.00196 **2022**, 1.
- [23] C. D. Amico, A. Houard, S. Akturk, Y. Liu, J. Le Bloas, M. Franco, B. Prade, A. Couairon, V. T. Tikhonchuk, A. Mysyrowicz, *New J. Phys.* **2008**, 10, 013015.
- [24] M. Clerici, M. Peccianti, B. E. Schmidt, L. Caspani, M. Shalaby, M. Giguère, A. Lotti, A. Couairon, F. Légaré, T. Ozaki, D. Faccio, R. Morandotti, *Phys. Rev. Lett.* **2013**, 110, 253901.
- [25] A. D. Koulouklidis, C. Gollner, V. Shumakova, V. Y. Fedorov, A. Pugžlys, A. Baltuška, S. Tzortzakis, *Nat. Commun.* **2020**, 11, 292.
- [26] T.-J. Wang, S. Yuan, Y. Chen, S. L. Chin, *Chinese Opt. Lett.* **2013**, 11, 011401.
- [27] S. Tzortzakis, G. Méchain, G. Patalano, Y.-B. André, B. Prade, M. Franco, A. Mysyrowicz, J.-M. Munier, M. Gheudin, G. Beaudin, P. Encrenaz, *Opt. Lett.* **2002**, 27, 1944.
- [28] A. Proulx, A. Talebpour, S. Petit, S. L. Chin, *Opt. Commun.* **2000**, 174, 305.
- [29] H. Hamster, A. Sullivan, S. Gordon, W. White, R. W. Falcone, *Phys. Rev. Lett.* **1993**, 71, 2725.
- [30] S. Varma, Y.-H. Chen, H. M. Milchberg, *Phys. Rev. Lett.* **2008**, 101, 205001.
- [31] F. Calegari, C. Vozzi, S. Gasilov, E. Benedetti, G. Sansone, M. Nisoli, S. De Silvestri, S. Stagira, *Phys. Rev. Lett.* **2008**, 100, 123006.
- [32] J. Papeer, M. Botton, D. Gordon, P. Sprangle, A. Zigler, Z. Henis, *New J. Phys.* **2014**, 16, 123046.
- [33] Y.-H. Cheng, J. K. Wahlstrand, N. Jhajj, H. M. Milchberg, *Opt. Express* **2013**, 21, 4740.
- [34] N. Jhajj, E. W. Rosenthal, R. Birnbaum, J. K. Wahlstrand, H. M. Milchberg, *Phys. Rev. X* **2014**, 4, 011027.
- [35] G. Point, C. Milián, A. Couairon, A. Mysyrowicz, A. Houard, *J. Phys. B At. Mol. Opt. Phys.* **2015**, 48, 094009.
- [36] S. Tzortzakis, B. Prade, M. Franco, A. Mysyrowicz, S. Hüller, P. Mora, *Phys. Rev. E* **2001**, 64, 057401.
- [37] A. Houard, V. Jukna, G. Point, Y.-B. André, S. Klingebiel, M. Schultze, K. Michel, T. Metzger, A. Mysyrowicz, *Opt. Express* **2016**, 24, 7437.
- [38] E. W. Rosenthal, I. Larkin, A. Goffin, T. Produit, M. C. Schroeder, J.-P. Wolf, H. M. Milchberg, *Opt. Express* **2020**, 28, 24599.
- [39] M. Scheller, N. Born, W. Cheng, P. Polynkin, *Optica* **2014**, 1, 125.
- [40] P. J. Skrodzki, M. Burger, L. A. Finney, R. Nawara, J. Nees, I. Jovanovic, *Opt. Lett.* **2021**, 46, 3777.
- [41] J. R. Koehler, F. Köttig, B. M. Trabold, F. Tani, P. S. J. Russell, *Phys. Rev. Appl.* **2018**, 10, 064020.
- [42] A. Goffin, I. Larkin, A. Tartaro, H. M. Milchberg, arXiv 2208.04240 **2022**.
- [43] P. Walch, B. Mahieu, L. Arantchouk, Y.-B. André, A. Mysyrowicz, A. Houard, *Appl. Phys. Lett.* **2021**, 119, 264101.
- [44] J. Isaacs, B. Hafizi, L. A. Johnson, E. W. Rosenthal, L. Mrini, J. Peñano, *Opt. Express* **2022**, 30, 22306.
- [45] M. Lenzner, J. Yeak, K. Kremeyer, in *4th Inter. Symp. on Filamentation COFIL*, Tucson, AZ **2012**.
- [46] M. Lenzner, J. Yeak, K. Kremeyer, in *2013 Conf. on Lasers & Electro-Optics Europe & Inter. Quantum Electronics Conf. CLEO EUROPE/ IQEC*, Optical Society of America, Munich, Germany **2013**.
- [47] A. Rastegari, J.-C. Diels, *APL Photonics* **2021**, 6, 060803.
- [48] A. D. Koulouklidis, C. Lanara, C. Daskalaki, V. Y. Fedorov, S. Tzortzakis, *Opt. Lett.* **2020**, 45, 6835.
- [49] A. Higginson, Y. Wang, H. Chi, A. Goffin, I. Larkin, H. M. Milchberg, J. J. Rocca, *Opt. Lett.* **2021**, 46, 5449.
- [50] E. F. Toro, M. Spruce, W. Speares, *Shock Waves* **1994**, 4, 25.
- [51] E. F. Toro, in *Riemann Solvers And Numerical Methods For Fluid Dynamics: A Practical Introduction*, Springer Science & Business Media, Switzerland AG **2009**.
- [52] S. Xu, X. Sun, B. Zeng, W. Chu, J. Zhao, W. Liu, Y. Cheng, Z. Xu, S. L. Chin, *Opt. Express* **2012**, 20, 299.
- [53] S. C. Rae, K. Burnett, *Phys. Rev. A* **1992**, 46, 1084.
- [54] X. M. Zhao, J.-C. Diels, C. Y. Wang, J. M. Elizondo, *IEEE J. Quantum Electron.* **1995**, 31, 599.